Biosensors and Bioelectronics 142 (2019) 111524

Contents lists available at ScienceDirect

Biosensors and Bioelectronics

journal homepage: www.elsevier.com/locate/bios

Dual-quenching electrochemiluminescence resonance energy transfer system from Ru–In_2S_3 to α-MoO_3-Au based on protect of protein bioactivity for procalcitonin detection

Jingwei Xue[a], Lei Yang[a], Yue Jia[a], Yong Zhang[a], Dan Wu[a], Hongmin Ma[a], Lihua Hu[a,*], Qin Wei[a,**], Huangxian Ju[a,b]

[a] Key Laboratory of Interfacial Reaction & Sensing Analysis in Universities of Shandong, School of Chemistry and Chemical Engineering, University of Jinan, Jinan, 250022, PR China

[b] Key Laboratory of Analytical Chemistry for Life Science, School of Chemistry and Chemical Engineering, Nanjing University, Nanjing, 210023, PR China

ARTICLE INFO

Keywords:
Electrochemiluminescence
Bioactivity-protection
Dual-quenching
Site-oriented antibody immobilization
Indium sulfide

ABSTRACT

Herein, a highly efficient dual-quenching biosensor based on electrochemiluminescence resonance energy transfer (ECL-RET) is designed utilizing Ru–In_2S_3 as ECL acceptor and α-MoO_3-Au as ECL donor. Compared α-MoO_3-Au with pure α-MoO_3, the overlapping peak area between ECL emission of Ru–In_2S_3 and UV–vis spectra of α-MoO_3-Au is increased, indicated better quenching effect is obtained. Hollow In_2S_3 and α-MoO_3-Au both have huge specific surface area to host a large amount of luminophores and antibodies. Moreover, HWRGWVC (H7) as specific capturer is adopted to achieve site-oriented antibody immobilization, which not only maintain antibody activity, but greatly improve the incubation process of antibodies, thus promoting the sensitivity of the biosensor. It's worth mentioning that the effect of over-potential on protein activity was proved in this work. The proposed biosensor obtained sensitive response by using PCT as a target with wide linear range from 0.0001 to 50 ng/mL and low detection limit of 12.49 fg/mL (S/N = 3), indicating its potential in the detection of biomarkers. Importantly, a novel ECL-RET pair of Ru–In_2S_3 (donor)/α-MoO_3-Au (acceptor) is firstly developed, which opened an efficient way for highly sensitive detection of antibody in disease clinical and diagnosis analysis.

1. Introduction

Electrochemiluminescence (ECL), one luminous progress obtained from the excited luminophores (Shi et al., 2012), has gradually attracted widespread focus on account of its low ratio of signal-to-noise (S/N), high sensitivity (Xue et al., 2019), and simplified instrument operation, etc. The application of ECL technique in immunoassay field requires that immune molecules can maintain high bioactivity in whole process, which should be the core of improving immune recognition and reducing detection limit (David and Richter, 2002). In view of this, many researchers have turned their attention to explore more ECL luminophore with good biocompatibility for replacing toxic carriers (Luo et al., 2018), such as Cd-based compound (Chen et al., 2018a). However, this strategy cannot fundamentally protect immune molecules, as reason that antigen or antibody can be inactivated by complexing reaction with heavy metal ions (Nahar and Tajmir-Riahi, 1996) and completely oxidized in excessive cyclic voltammetry scan (Bruce and Richter, 2002). Compared with traditional ECL reagents (Feng et al., 2016), such as g-C_3N_4, luminol, Ru $(bpy)_3^{2+}$ and so on (Tian et al., 2018), many novel semiconductors luminophore need higher oxidation potential to meet requirements of high-energy-state, which hinder their expansion to immunoassay. About this aspect, some corresponding proofs were made in this paper. Thus, the activity of detected proteins should be focused more. With the advantages of low excited potential and ultrahigh ECL efficiency (Wu et al., 2018), Ru $(bpy)_3^{2+}$ is still one of the most suitable ECL emitters in immunoassay (Liu et al., 2018b) on the selection of luminescent materials. However, excellent water solubility makes it difficult to immobilize on the electrode surface (Du et al., 2018a). Therefore, one of the problems should be solved was searching suitable materials for achieving abundant Ru $(bpy)_3^{2+}$ immobilization should be focused (Zhao et al., 2019).

Metal sulfide is widely used as a kind of active photocatalyst (Hao

* Corresponding author.
** Corresponding author.
E-mail addresses: hulihua1206@163.com (L. Hu), sdjndxwq@163.com (Q. Wei).

https://doi.org/10.1016/j.bios.2019.111524
Received 12 June 2019; Received in revised form 7 July 2019; Accepted 16 July 2019
Available online 19 July 2019
0956-5663/

et al., 2018) due to its unique electronic structure, adjustable optical properties and appropriate band gap and edge (Xiao et al., 2018). However, it has potential applications in ECL and other fields because of its good conductivity and catalysis (Du et al., 2018b). Meanwhile, the structure of 2D nanosheets is conducive to reducing the carrier diffusion length and supplying high surface area, thus accelerating transfer rate of electrons and providing abundant active sites for the redox reaction. The hollow microstructures (Jing et al., 2018) own the structure-dependent advantages when compared with solid structures (Chen et al., 2018b). Their internal cavities can also promote electron transfer by reducing the diffusion length from the body to the surface, and provide large specific surface area to improve the concentration of adsorbate. In this work, 3D hollow In_2S_3 nanotubes with multiple shell layers (In_2S_3 HNTs) possessing both hollow structure to accelerate electron flow and multilayer structure with a large specific surface area are successfully prepared by self-templated strategy (Wang et al., 2017). In_2S_3 HNTs not only increase the adsorption amount of Ru $(bpy)_3^{2+}$, but also effectively improve the electron transfer efficiency to make it obtain good stability and suitable intensity.

MoO_3 is an environmentally friendly n-type semiconductor metal oxide (Mai et al., 2010), which has been widely studied and applied in catalyst, adsorption, sensor (Mandal et al., 2018) and other fields. Up to now, studies on MoO_3 mainly focus on low-dimensional MoO_3 structures, such as nanosheet, nanostrip, nanorod and nanoparticle (Liu et al., 2018a), while reports on multi-level structure of MoO_3 are relatively few because of the complicated preparation (Li Hua et al., 2019). Therefore, it is necessary to apply multistage MoO_3 with simple preparation and good performance in the sensing field. In this work, hollow porous α-MoO_3 nanospheres (α-MoO_3 HNSs) composing with nanoparticles are successfully prepared through hydrothermal and roasting synthesis.

Fortunately, the ultraviolet absorption (UV–vis) spectra of α-MoO_3 overlaps with ECL emission of Ru $(bpy)_3^{2+}$ effectively was found, and the overlap area increased after α-MoO_3 compounded with gold nanoparticles (Au NPs). The dual quenching effect not only achieves better quenching efficiency but also effectively improves the sensitivity of biosensor. In order to further improve the sensitivity of the immunosensor, this work also uses the small peptide ligands assisted to realize site-directed immobilization of antibodies (Makaraviciute and Ramanaviciene, 2013).

It is worth noting the second problem that except the suitable scanning potential, the antigenic-recognition ability of biosensors mainly depends on the bioactivity of immobilized antibodies. If the active section N-terminus Fab fragment of antibody applies to bonding with the materials, the activity of the antibodies would decrease or even disappear and the binding efficiency of antigens and antibodies would also be greatly reduced. In order to avert stochastic immobilization and improve the availability of antibodies which need to bind with antigen, it is greatly significant to achieve site-directed immobilization. Currently, the use of small peptide ligands to achieve effective site-directed immobilization of antibody has attracted much attention. It's worth mentioning that HWRGWV hexapeptide (Dostalova et al., 2016) which holds superiority of low cost, easy preparation, stability has been verified to specifically interact with the amino acids of antibody Fc fragment with high affinity. Thus, HWRGWV possesses great potential for applications in site-directed antibody immobilization of ECL immunosensor. In this work, HWRGWVC heptapeptide (H7) is obtained by modifying a cysteine on C-terminus of HWRGWV hexapeptide which could provide –SH to combine with materials. It's worth mentioning that the sensitivity and the antibody binding capacity are both further improved when comparing with previous similar work (Jia et al., 2019).

Nowadays, many previous works of similar sensors have been achieved outstanding results. For example, wearable sensors (Jin et al., 2016) could detect Parkinson's disease, stroke (Taylorpiliae et al., 2015) and other diseases by monitoring physical factors such as exercise, blood pressure and blood sugar. In view of these, In_2S_3 HNTs were successfully prepared as substrate to adsorb Ru $(bpy)_3^{2+}$ (Ru–In_2S_3) for achieving great ECL intensity. α-MoO_3 HNSs were prepared by hydrothermal and calcining reactions and compounded with Au NPs by electrostatic interaction to achieve the effect of dual-quenching. H7 combined with materials through amide bond (with Ru–In_2S_3) and Au–S bond (with α-MoO_3) which could capture the Fc fragment of the antibody to achieve effective antibody immobilization. Electrochemiluminescence resonance energy transfer (ECL-RET) from Ru–In_2S_3 to α-MoO_3-Au would occur and further confirmed by testing the overlap between ECL emission of Ru–In_2S_3 and UV–vis spectra of α-MoO_3-Au. PCT was used as the target for the test, and a dual-quenching immunosensor with antibody site-directed immobilization based on RET from Ru–In_2S_3 to α-MoO_3-Au was constructed, which provided a basis for sensitive analysis of biomarkers and contributed to develop personalized and precision medicine in years to come.

2. Experimental section

2.1. Synthesis of In_2S_3 HNTs

Prior to preparation, the precursor was prepared firstly. In-MOF hexagonal prisms were synthesized according to a reported method (Wang et al., 2017) with some modifications. The basic steps are as follows: 4.5 mg of $In(NO_3)_3{\cdot}xH_2O$ and 5.5 mg of 1,4-benzenedicarboxylic acid were mixed and dissolved in 2 mL of Dimethyl Formamide (DMF) and stirred for 10 min. Next, the resultant solution was heated at 120 °C for 30 min. After cooling down, the white precipitate was washed with ethanol for three times and dried at 60 °C. The obtained In-MOF hexagonal prisms were added into 40 mL of ethanol solution containing 200 mg of thiourea, and stirred for 2 min. Then, the resultant mixture was transferred into one 80 mL Teflon-lined autoclave and maintained at 180 °C for 3 h. After cooling down to room temperature, yellow precipitate was filtrated and washed with ethanol and ultrapure water for three times, respectively, and dried at 60 °C for further use.

2.2. Synthesis of Ru–In_2S_3 nanocomposite

2 mg of In_2S_3 HNTs were accurately dissolved into the mixture of 1 mL deionized water and 1 mL of 1×10^{-3} M Ru $(bpy)_3^{2+}$. The obtained solution was oscillated for 12 h in dark at the room temperature. After centrifugation at 8000 rpm, Ru–In_2S_3 was obtained and then it was re-dissolved into 1 mL of distilled water.

2.3. Preparation of α-MoO_3-Au nanocomposite

First at all, α-MoO_3 was synthesized according to previous report (Li Hua et al., 2019) with a slight modification. 0.14 g of $C_{10}H_{14}MoO_6$ was dissolved into 30 mL of N-butyl alcohol under ultrasound for 10 min to make the solid evenly dispersed into the solvent. Then under magnetic stirring, 5 mL of 1 M HNO_3 was added into the mixture by drop, and then stirred for 1 h. The obtained mixture was then shifted into a 50 mL Teflon-lined autoclave and heated at 220 °C for 12 h, followed by cooling down to room temperature. The precipitate shown up in black was washed by deionized water and anhydrous ethanol for 5 times in turn. After drying at 60 °C for 5 h, the precursor MoO_2 was obtained, and then MoO_2 was heated at 400 °C for 3 h under air atmosphere. The obtained white powder indicated the successful synthesis of α-MoO_3. Additionally, 1 mL of $HAuCl_4$ (1%) and 10 mg PVP were assessed into the obtained composite solution under stirring for 10 h. Following by adding 4 mL of sodium citrate solution (50 mM) and 0.08 mg $NaBH_4$ into the mixture and stirring for 12 h, the α-MoO_3-Au was washed with anhydrous ethanol and ultrapure water. Finally, α-MoO_3-Au was re-dissolved into 1 mL of PBS (pH 7.4) for use after centrifugation. The α-MoO_3-Au-H7-Ab_2 bioconjugate was prepared soon (Supplementary Material).

2.4. Fabrication of the immunosensor

Glassy carbon electrode (GCE) (Φ = 4 mm) was polished by utilizing alumina (Al_2O_3) powder to make mirror-like surface with granularity of 0.05 μm and 0.03 μm and followed by ultrasonic with ultrapure water and ethanol. It's worth noting that the modified electrode should be rinsed thoroughly with 10 mM PBS (pH 7.4) to get rid of the unabsorbed species after each step below (Yang et al., 2018). Firstly, the bare GCE was modified with 6 μL of Ru–In_2S_3 suspension, and dried at room temperature. Then, GCE/Ru–In_2S_3 was immersed into PBS containing 0.1 M NaCl and 3 mM mercaptoacetic acid for 5 h at 4 °C to introduce carboxyl groups and carboxyl groups were activated by immersing GCE/Ru–In_2S_3 in EDC/NHS (Zhou et al., 2016). After that, the electrode was dipped in H7 (50 ng/mL) solution to capture H7 via amide bond at 4 °C for 60 min. After that, the electrode was steeped in BSA (0.1%) for 30 min at room temperature. Then, the electrode was dipped into the Ab_1 (5 μg/mL) to incubate at 4 °C for 50 min. Next, 6 μL of PCT with different concentrations were incubated at 37 °C for 40 min. Next, 3 μL of BSA (0.1%) was dropped on the surface to hinder the non-specific active sites and dried into a film. Subsequently, different concentrations of PCT were incubated on the above surface following by drying at 4 °C (Wu et al., 2018). Followed by modifying 6 μL of α-MoO_3-Au-Ab_2 and dried. This ECL biosensor was constructed and conserved at 4 °C for next steps finally. In Scheme 1, the construction process of the proposed ECL biosensor was shown.

2.5. ECL measurements of immunosensor

In this work, the ECL strategy was tested by three-electrode system (Supplementary Material). Cyclic voltammetry (CV) was applied from 0 to 1.15 V to the electrochemical measurement at scanning rate of 0.12 V/s (Huang et al., 2017). The measurement was worked in 10 mL of 1/15 M PBS (pH 7.6) containing 50 mM TPA with the voltage of photomultiplier tube (PMT) at 600 V to optimize conditions and detect the ECL responses to PCT with a series of different concentrations.

3. Results and discussion

3.1. Material characterization

Scanning electron microscope (SEM) images showed the average length (Fig. 1A) and diameter of In-MOF hexagonal prisms (inset of Fig. 1A) are about 550 nm and 400 nm, respectively (Qin et al., 2010). As shown in Fig. 1B, the surface of the In_2S_3 hollow nanotubes are composed of randomly assembled ultrathin nanosheets. In_2S_3 HNTs were further demonstrated by transmission electron microscopy (TEM). In Fig. 1C, the well-defined hierarchical hollow structure with shell thickness of about 120 nm was presented clearly. Energy dispersive spectrometer (EDS) of In_2S_3 was shown in Fig. S1A, the existence of In and S elements could be observed. XRD (Fig. S1B) was also applied to characterize In_2S_3 crystallization. Specific peaks of three planes were found at 33.445°, 47.995° and 70.116°, which corresponded to the (200), (220) and (400) planes of In_2S_3 HNTs, respectively (JCPDS Card NO. 05–0731). Besides, the existence of the representative lattice was proved by high-resolution transmission electron microscopy (HRTEM) (Fig. 1D). Furthermore, N_2 adsorption isotherms of In_2S_3 HNTs and the pore size distribution curve of the derived from the adsorption branches of the isotherms by using the Barrett-Joyner-Halenda (BJH) method were also tested, the details were shown in Supplementary Material.

Moreover, α-MoO_3 HNSs and MoO_3–Au nanocomposite were confirmed by the similar means of representation. SEM images showed the average diameters of the precursor MoO_2 (Fig. 1E) and α-MoO_3 (Fig. 1F) are both about 480 nm. As shown in inset of Fig. 1F, the α-MoO_3 HNSs presented a hollow porous structure which was comprised of many nanoparticles. α-MoO_3 was further verified by TEM image in Fig. 1G, which presented the well-defined porous structure with thicker shell thickness of about 80 nm. EDS of α-MoO_3 was shown in Fig. S1C, it could be observed the existence of Mo and O elements. After the precursor MoO_2 changed into α-MoO_3 successfully by calcining. XRD (Fig. S1D) was applied to characterize the crystallization of MoO_2 and α-MoO_3. Specific peaks of different planes of MoO_2 were found at 26.033°, 31.784°, 37.025°, 49.468°, 53.512°, 60.197°, 66.659° and 73.248°, which corresponded to the (−111), (111), (−202), (−301), (−312), (031), (−402) and (413) planes, respectively (JCPDS Card NO. 32–0671). The diffraction pattern for theα-MoO_3 had five broad peaks at 23.328°, 25.704°, 27.334°, 54.127° and 58.804°, corresponding to the (110), (040), (021), (221) and (180) planes, respectively (JCPDS Card NO. 05–0508). The existence of the representative lattice was also proved by HRTEM (Fig. 1H). In order to prove the successful composition of α-MoO_3-Au, SEM image and its corresponding mapping (Fig. 1I) were utilized to present α-MoO_3-Au preparing by the in-situ reduction not only its morphology but also the existence of Mo, O, Au

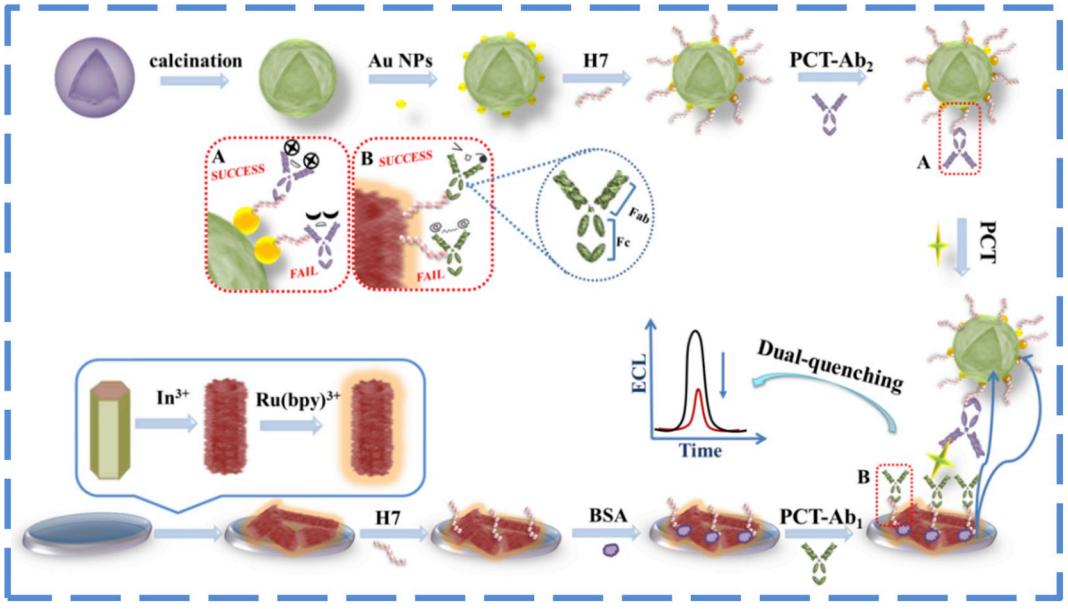

Scheme 1. Schematic representation of the fabrication of immunosensor.

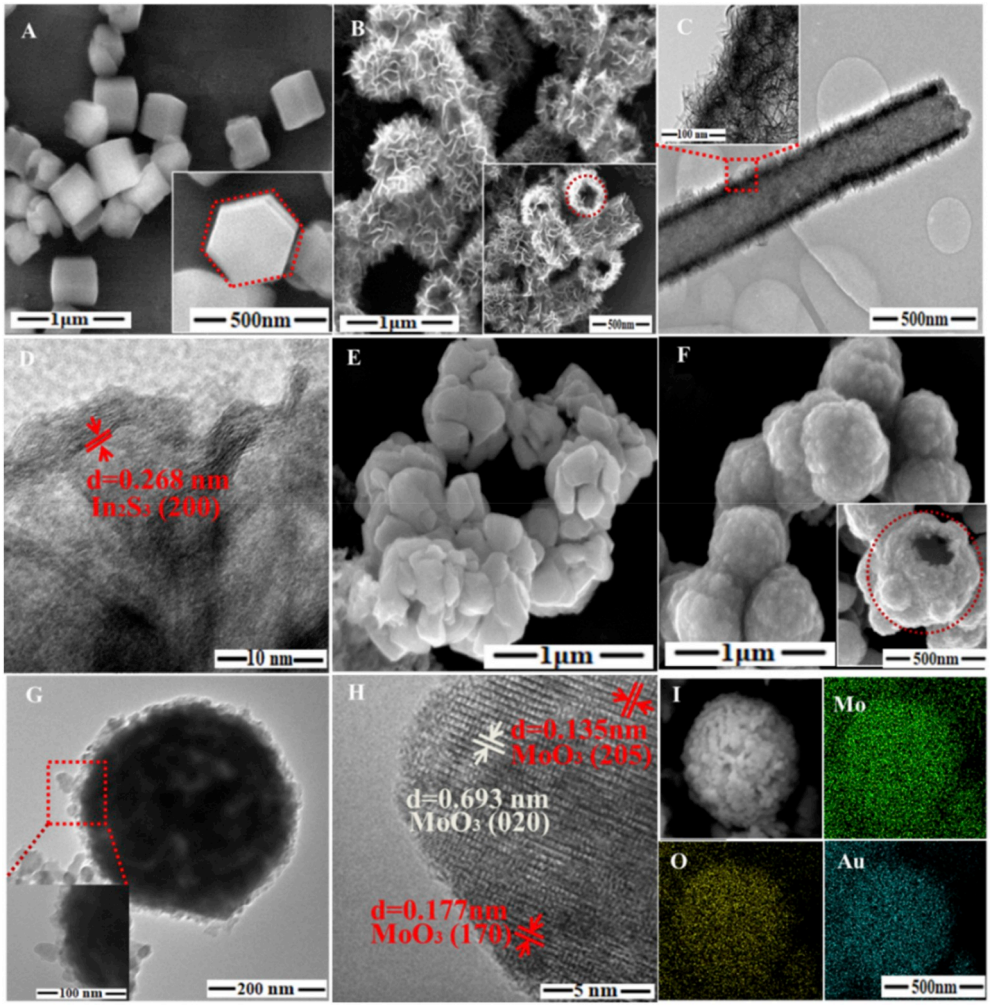

Fig. 1. SEM image of In-MOF (A). SEM (B), TEM (C) and HRTEM (D) images of In_2S_3. SEM images of MoO_2 (E) and α-MoO_3. TEM (G) and HRTEM (H) images of α-MoO_3. SEM image and the corresponding mapping of α-MoO_3-Au (I).

elements. It was further characterized by TEM (Fig. 1SE) and EDS (Fig. 1SF), which provide another intuitive proof information for α-MoO_3-Au composite. All of results indicated the preparation of In_2S_3, α-MoO_3 and α-MoO_3-Au in this work was successful.

3.2. Analysis of PCT bioactivity and site-oriented antibody capture

The activity of the immune molecules can be reflected by observing the change of conformation utilizing CD spectra. The CD spectra of PCT with 0.5 mg/mL stimulated by different potential (Fig. 2A). All of the PCT samples were bubbled with high-purity nitrogen for 30 min to empty oxygen and ensure the experimental results were not affected by superoxide radical and other reactive oxygen species. Subsequently, the PCT samples saturated with high-purity nitrogen were scanned using CV model in a three-electrode system by adjusting the potential (0–1 V, 0–1.2 V, 0–1.5 V, 0–2 V) or scanning time (0.5 min, 1 min, 2 min, 5 min) at 4 °C. Furthermore, the other experimental conditions were consistent. The data obtained are expressed as mean residue ellipticity (MRE). The samples were diluted with PBS (0.1 M), which is without any absorption (curve a), instead other curves showed the analogous β-sheet conformation thanks to the characteristic peaks appeared at 213 nm and 195 nm. Concretely, the primordial sample without any dispose exhibited maximum mean residue ellipticity (MRE) (curve b), which could be regarded as reference for analyzing other samples. Followed by scanning under the potential of 0–1 V and 0–1.2 V, the MRE of PCT decreased slightly (curve c and d), which could be explained by the medium-level potential damage of secondary structure with slight change of conformation. Furthermore, the CD intensity of PCT exhibited a trend of rapid decline (curve e) when the potential range was broadened to 0–1.5 V. Fabulously, the MRE of PCT decreased by nearly half (curve f) compared to the original sample when the excitation potential was 0–2 V. Besides, the effect of stimulated time on antibody bioactivity was explored under 0–1.15 V by CD (Fig. 2B). The results represented the CD spectrum of PCT with 0.5 mg/mL stimulated for 30 s which can obtain the maximum MRE (curve a). Additionally, curve (b, c) and (d) respectively expressed the CD spectra of PCT with stimulation for 1, 2 and 5 min. The results proved that the low-potential in a short time cannot have a significant impact but the long-term cyclic voltammetry scan not, which indicated that the degree of the potential and the scanning time can lead to irreversible damage of protein, especially the potential over 1.2 V or longer time galvanism. In view of these, more attention should be paid to protect the bioactivity of protein rather than widely explore ECL materials in immunoassay. The favorable potential of Ru $(bpy)^{3+}$ and its excellent stability by using very short time to reach become its great advantages.

The coupling of H7 with In_2S_3 could be analyzed by RP-HPLC (Fig. S2A). H7 (50 ng/mL) was measured at 3.6 min (curve black), while the peak area had diminution significantly after incubated with In_2S_3 and α-MoO_3-Au (curve red and curve blue). This result could prove the successful incubation of H7 with Ru–In_2S_3 and α-MoO_3-Au owing to amide bond and Au–S bond, respectively. Moreover, H7 with gradient concentrations were detected by using RP-HPLC and the obtained

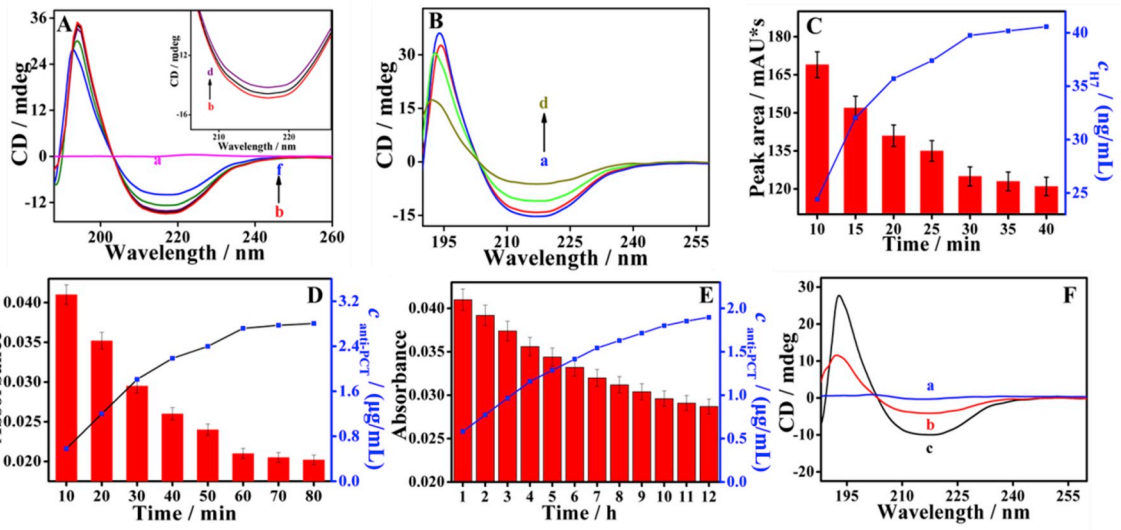

Fig. 2. (A) CD spectra of PCT with 0.5 mg/mL stimulated by different potential (A) and scanning time (B). HPLC results (C) of uncaptured H7 (50 ng/mL) coupling with Ru–In_2S_3 from 10 to 40 min (left red histogram) and the corresponding calculated adsorption amount of H7 (right blue line chart). (D) UV–vis absorption of uncaptured PCT-Ab_2 by H7 with a time range from 10 to 80 min (left red histogram) and the corresponding calculated adsorption amount of PCT-Ab_2 (right blue line chart). (E) UV–vis absorption of uncaptured PCT-Ab_2 without H7 (only by Au–N adsorption) in time range of 1–12 h. (F) CD spectra of pure H7 (a), α-MoO_3-Au-Ab_2 (b), α-MoO_3-Au-H7-Ab_2 (c). (For interpretation of the references to colour in this figure legend, the reader is referred to the Web version of this article.)

values could draw the corresponding standard curve. The regression equation P = −13.0313 + 110.7868 × lg *c* (R^2 = 0.9958) (Fig. S2B). Then, 1 mL of Ru–In_2S_3 solution was blended with H7 (50 ng/mL) and shocked at 4 °C for a series of different time. The supernatants were tested by utilizing RP-HPLC (treat α-MoO_3-Au and H7 in the same way) after centrifugation. As shown in Fig. 2C, the decline rate decreased and leveled off at 30 min. According to the regression equation, Peak Area = 125.3, and the connected amount of H7 was calculated to be about 40.17 ng, which indicated that approximately 40.17 ng of H7 (80.32%) could be captured in 30 min via amide bond. Using the same processing and calculation method, it could be obtained that α-MoO_3-Au could complete capture of about 39.62 ng of H7 (79.21%) in 30 min via Au–S bond (Fig. S2C). After coupled with H7 for 30 min, 1 mL of Ab_2 (5 μg/mL) was accessed into for different incubation time at 4 °C. The collected supernatants were analyzed by UV–vis and the absorbance leveled off at 60 min (Fig. 2D). The obtained absorbance A = 0.0221, the connected amount of antibody was calculated at 2.74 μg according to the obtained regression equation (Fig. S2D).

As comparison, α-MoO_3-Au modified without H7 was directly compounded with 1 mL of Ab_2 (5 μg/mL) for a series of incubation time at 4 °C. During this step, antibody could capture with α-MoO_3-Au only via Au–N bond. When the incubation time attained to 12 h (Fig. 2E), the obtained absorbance A = 0.0282, the connected amount of antibodies was calculated to be about 1.98 μg, which was similar but a little less than that using H7 method. However, it is worth mentioning that compared with the two methods, the latter one took more than 10 times as long as the former. Therefore, H7 also played a significant role in shortening incubation time of antibodies and improving the incubation efficiency. In order to compare the biological activity of Ab_2 using H7 to without H7, it was confirmed by CD spectra. The results of CD spectra presented a significant difference due to using site-oriented or random immobilization method of antibodies (Fig. 2F). All of results could be indicated the activity of Ab_2 obtained by using H7 was maintained better than that gained by Au–N, which highlighted the important role of H7 application in the maintenance of antibody activity.

3.3. Mechanism Investigation of the dual-quenching system

In this work, the Ru $(bpy)_3^{2+}$ adsorbed around In_2S_3 worked high anodic emission light with the existing co-reactant, tripropylamine (TPA) at the voltage range from 0 to 1.15 V. Two possible mechanism routes should be happened in this ECL system of Ru $(bpy)_3^{2+}$ − TPA. In route 1, one of the possible mechanism to gain excited-state Ru $(bpy)_3^{2+}$ was shown clearly. Firstly, in a low-potential ECL, TPA was oxidized to $TPA^{\cdot+}$ directly and then deprotonated to TPA·. Ru $(bpy)_3^{2+}$ was reduced by TPA· (radical species) to product Ru $(bpy)_3^{+}$, which would react with $TPA^{\cdot+}$ (oxidative species) to produce Ru $(bpy)_3^{2+}$*. In route 2, another conceivable mechanism would be taken place at high-potential. Firstly, Ru $(bpy)_3^{3+}$ was obtained by oxidizing Ru $(bpy)_3^{2+}$ directly and then further reacted with TPA· to form Ru $(bpy)_3^{2+}$*. Additionally, an alternative mechanism for producing Ru $(bpy)_3^{2+}$* at higher potential would be increased when Ru $(bpy)_3^{3+}$ produced from route 2 reacted with Ru $(bpy)_3^{+}$ obtained from route 1 to form Ru $(bpy)_3^{2+}$*. In_2S_3 as the substrate could capture more Ru $(bpy)_3^{2+}$ on the surface of electrode to generate more Ru $(bpy)_3^{2+}$*, thus obtaining large and stable ECL signals.

Route 1

$$TPA - e \rightarrow TPA^{\cdot+}$$

$$TPA^{\cdot+} - H^{+} \rightarrow TPA^{\cdot}$$

$$TPA^{\cdot} + Ru(bpy)_3^{2+} \rightarrow Ru(bpy)_3^{+} + product$$

$$Ru(bpy)_3^{+} + TPA^{\cdot+} \rightarrow Ru(bpy)_3^{2+}* + product$$

$$Ru(bpy)_3^{2+}* \rightarrow Ru(bpy)_3^{2+} + hv$$

Route 2

$$Ru(bpy)_3^{2+} - e \rightarrow Ru(bpy)_3^{3+}$$

$$TPA - e \rightarrow TPA^{\cdot+}$$

$$TPA^{\cdot+} - H^{+} \rightarrow TPA^{\cdot}$$

$$Ru(bpy)_3^{3+} + TPA^{\cdot} \rightarrow Ru(bpy)_3^{2+}*$$

$$Ru(bpy)_3^{2+}* \rightarrow Ru(bpy)_3^{2+} + hv$$

The dual-quenching mechanism of α-MoO_3-Au (acceptor) towards Ru–In_2S_3 (donor) system was mainly attributed to the existence of RET between two of them. Satisfactory overlap was investigated and found between the ECL emission of Ru–In_2S_3 (curve blue) and UV–vis spectroscopy of α-MoO_3 or α-MoO_3-Au (Fig. 3A). Compared α-MoO_3-Au

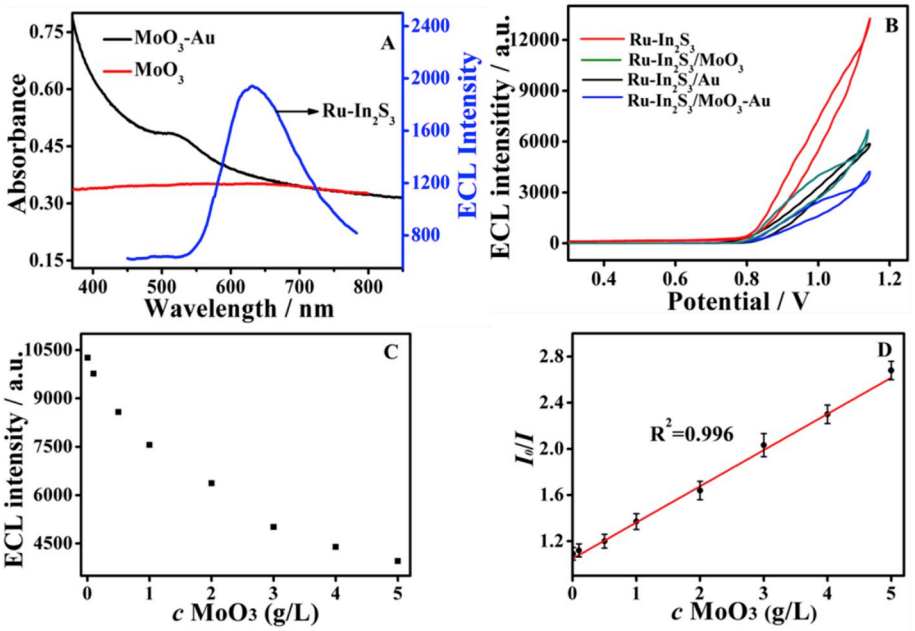

Fig. 3. (A) ECL spectra of Ru–In_2S_3 (a), UV–vis absorption of α-MoO_3 and α-MoO_3-Au (b), (B) ECL behavior of Ru–In_2S_3–H7-Ab_1/BSA/PCT (a), Ru–In_2S_3–H7-Ab_1/BSA/PCT/α-MoO_3 (b), Ru–In_2S_3–H7-Ab_1/BSA/PCT/Au (c), Ru–In_2S_3–H7-Ab_1/BSA/PCT/α-MoO_3-Au (d), (C) ECL of Ru–In_2S_3 in the existing of 0, 0.1, 0.5, 1, 2, 3, 4 and 5 g/L α-MoO_3-Au. (D) Calibration curve for α-MoO_3-Au detection in pH = 7.6 PBS containing 50 mM TPA on Ru–In_2S_3.

(curve black) with α-MoO_3 (curve red), the UV–vis absorption peak was wider, which based for enhancing of overlap and effect of quenching. As a result, the quenching effect of α-MoO_3 was increased by compositing Au NPs. Layer of GCE/Ru–In_2S_3–H7-Ab_1/BSA/PCT electrode was applied as the elementary probes (curve red) (Yang et al., 2011). Then, α-MoO_3 (curve green), Au NPs (curve black) and α-MoO_3-Au (curve blue) were further modified on electrode surface, respectively. In Fig. 3B, the quenching effect of α-MoO_3-Au was more satisfied than that of pure α-MoO_3 or Au. Also, α-MoO_3-Au-Ab_2 bedecking to GCE was detected, the ECL intensity decrease a little bit because the antibody further blocked the electron transfer on the electrode surface. For further confirmation, the ECL quenching towards Ru–In_2S_3 was explored at GCE with a series of concentrations of α-MoO_3-Au in 10 mL PBS (pH 7.6) containing 50 mM TPA. As concentration of α-MoO_3-Au increases, the ECL intensity decreased and the values were recorded in Fig. 3C. Based on an existing work, the plot of I_0/I versus a series of concentrations of α-MoO_3-Au was obtained in Fig. 3D, and it put a range of 0.05–5 g/L (R^2 = 0.996), indicating a quenching mechanism depicted by equation (Stern-Volmer). In this step, I and I_0 were on behalf of ECL intensity with α-MoO_3-Au and without, respectively. According to this plot, the quenching constant (K_{sv}) was measured at $3.136 \times 10^5\ g^{-1}$, while the excellent dual-quenching effect of α-MoO_3-Au on Ru–In_2S_3 was confirmed from all of these results.

3.4. Characterization of the immunosensor

First of all, the electrochemical active area of the electrode after substrate modification was calculated to describe the relative state of the electrode surface. GCE/Ru–In_2S_3 was tested by CV in 2.5 mM Fe $(CN)_6^{3-/4-}$ and 0.1 M KCl with different scanning speed range from 0.02 V/s to 0.4 V/s (Fig. 4A),. The standard curve was drawn with the reduction peak current i_{pc} as ordinate, and the scanning speed to the power 1/2 as abscissa to obtain the regression equation $i \times 10^{-6}(A) = -240.4(v^{1/2}/s^{1/2})-0.9904$ (Fig. 4B). It was further indicated that the electrode surface was only controlled by diffusion (Wang et al., 2019). According to Randles-Sovcik equation, the calculated effective electrochemical active area was 2.25 times of the actual area (The details were in the Supplementary Material), which was due to the large surface area of In_2S_3. It's worth mentioning that the increase of electrochemical active area is conducive to adsorption of more Ru $(bpy)_3^{2+}$, and at the same time, it also increases the catalytic site on the electrode and accelerates the rate of redox reaction on the electrode surface (Wang and Ma, 2018).

Besides, electrochemical impedance spectroscopy (EIS) was worked in 2.5 mM $[Fe(CN)_6]^{3-/4-}$ and 0.1 M KCl at different modified-electrodes for the fabrication characterization of the biosensor. As shown in Fig. 4C, the bare GCE only performed a small semicircle domain (curve a), which owned to the mass transfer process. When Ru–In_2S_3 was modified on the electrode, a little bigger arch than curve a (curve b) was shown distinctly, as a result of diffusion control and the impedance effect of nanomaterial itself. When H7 and Ru–In_2S_3 successfully immobilized and combined, the impedance value was only slightly increased (curve c). It was related to the small molecular structure of H7 itself. Then, Ab_1 (curve d), BSA (curve e) and PCT (curve f) was modified layer by layer, and the semicircle domain was becoming bigger and bigger, indicating the impedance value increased gradually owing to the protein hindrance. Particularly, the electron transfer resistance increased significantly after modified with α-MoO_3-Au-Ab_2 (curve g) because the antibody and quenching agent further blocked the electron transfer on the electrode surface. Herein, in order to observe the impedance further, the circuit was simulated by using the equivalent circuit element of simulation parameters (Table S1). Additionally, cyclic voltammetry (CV) and the ECL intensity were also performed for the above electrodes (Fig. S3 and Fig. 4D). All of the results indicated the proposed ECL biosensor was successfully constructed.

3.5. Analysis of PCT

The effective ECL-RET system between Ru–In_2S_3 and α-MoO_3-Au in this work was utilized to detect a series of PCT sensitively. Raw data and the standard regression curve were shown in Fig. 5A and Fig. 5B, which made ECL intensity I_{ECL} as Y-axis and log c as X-axis. Its equation of linear regression was $I_{ECL} = 4315.61–1909.96 \times \lg c$ (R^2 = 0.9905) with linear range of 0.0001 ng/mL to 50 ng/mL and detection limit of 12.49 fg/mL (S/N = 3). This work was compared with other related work to explain the advantage of the detection method (Table S2). Results obtained at this step put up lower detection limit and wider detection range of this immunosensor, which could offer significant direction for the detection of PCT and other biomarkers.

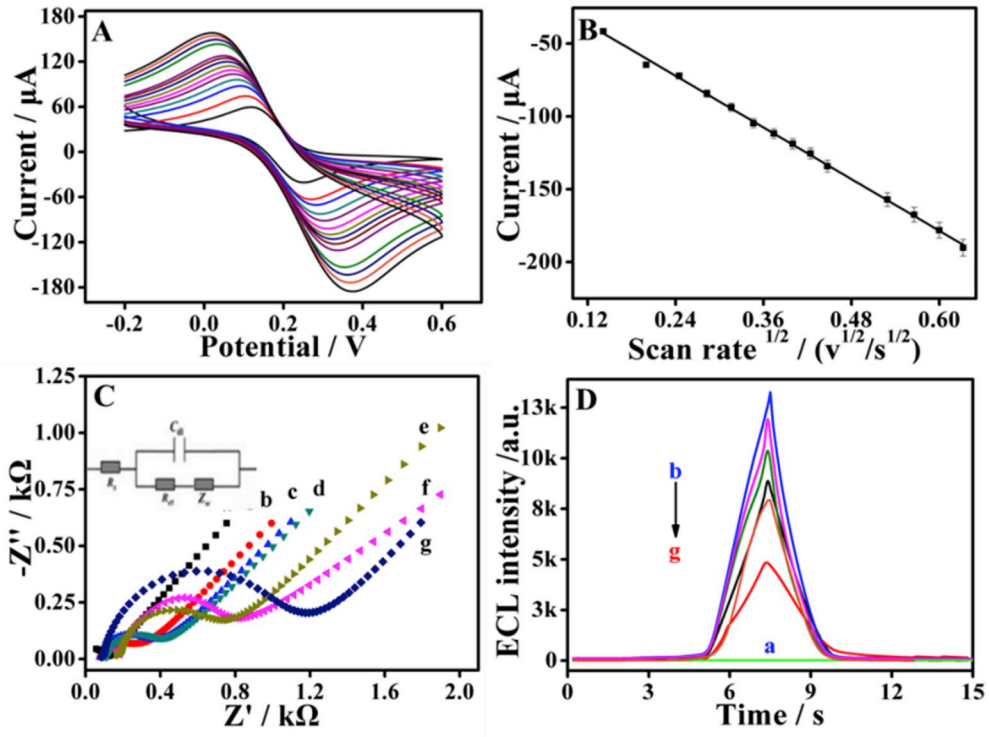

Fig. 4. CV curves (A) of GCE/Ru–In_2S_3 tested in 2.5 mM $Fe(CN)_6^{3-/4-}$ and 0.1 M KCl with different scanning speeds ranging from 0.02 V/s to 0.4 V/s and its corresponding standard curve (B). EIS responses (C) and ECL intensity (D) of immunosensor with different modified states: (a) bare GCE, (b) GCE/Ru–In_2S_3, (c) GCE/Ru–In_2S_3–H7, (d) GCE/Ru–In_2S_3–H7/BSA, (e) GCE/Ru–In_2S_3–H7/Ab_1/BSA, GCE/Ru–In_2S_3–H7/Ab_1/BSA/PCT, (g) GCE/Ru–In_2S_3–H7/Ab_1/BSA/PCT/α-MoO_3-Au-Ab_2.

3.6. Real sample analysis

SIRS refers to the systemic inflammatory response (body's response to multiple cytokines/inflammatory mediators). Endotoxin is the trigger of systemic inflammatory response (SIR), and there is no obvious cure for this disease. PCT, a typical biomarker of SIRS in serum, plays a vital role in the early realization of accurate and reliable diagnosis of SIRS. In obtained human serum, the concentration of PCT specimen was detected to be 3.06 ng/mL by utilizing biosensor constructed in this work. In order to verify the application of this immunosensor, the recovery rate of different PCT concentration was acquired by the standard recovery method (Table S3) with RSD under 3.6% and recovery range from 95.2% to 96.8% (n = 5). F-test was performed to judge whether there was a prominent difference in accuracy. F value calculated (Equation (1)) was under the theoretical one (F = 6.39 at confidence limits 95%), indicated the highly equivalent precisions of both methods. In the meantime, the proposed biosensor was assessed by ELISA kit with the human serum concentration sample for five times respectively. There was no significant difference between the average value of standard recovery method and ELISA. This dual-quenching system was also applied to evaluate by T-test (Equation (2)). These results are demonstrated in Table 1. The value of t was under 2.78 (P = 0.95, α = 0.05, f = 4), indicated the neglect of system error. The precision and accuracy can be ensured through both F-test and *t*-test.

$$F = \frac{S_{big}}{S_{little}} \quad (1)$$

$$t = \frac{|\bar{x} - \mu|}{s}\sqrt{n} \quad (2)$$

4. Conclusion

In summary, the effect of potential on protein bioactivity, had been raised and confirmed by CD spectra. Based on this, dual-quenching ECL-RET system with high sensitivity utilizing Ru–In_2S_3 as donor and α-MoO_3-Au as acceptor was constructed. α-MoO_3-Au in the proposed RET process, which could be the dual-quencher thanks to the quenching

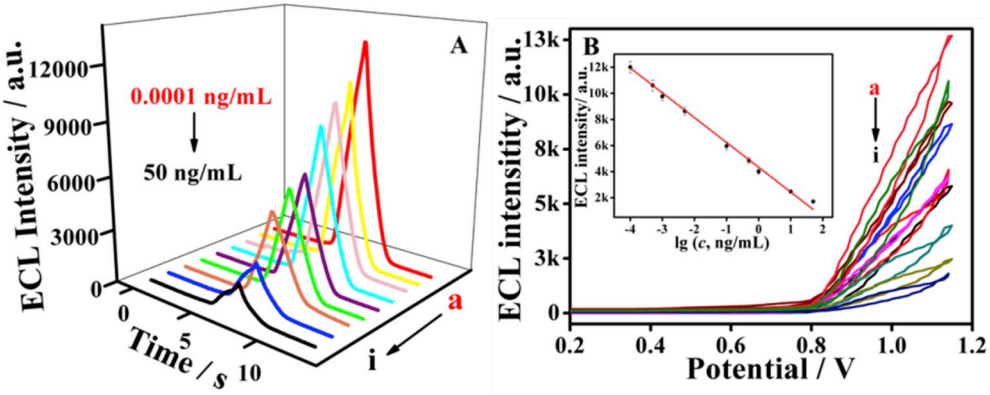

Fig. 5. ECL response of the biosensor to a series of different concentrations of PCT (a–i): 0.0001, 0.0005, 0.001, 0.005, 0.1, 0.5, 1, 10, and 50 ng/mL towards time (A) and potential (B), and the calibration curves (inset of B) of biosensor which detected in 10 mL of 1/15 M PBS (pH 7.6) containing 50 mM of TPA.

Table 1
F-test and *t*-test about serum samples analysis.

Sample content	ELISA (pg/mL)	Mean (pg/mL)	s	RSD (%)	This method (pg/mL)	Mean (pg/mL)	s	RSD (%)	F value	T test
PCT	6.09, 6.11, 6.03, 6.01, 6.10	6.07	0.04	0.74	6.19, 6.01, 6.13, 6.07, 6.15	6.11	0.07	1.16	1.75	1.28

"This method" is standard addition method above mentioned; the theoretical values at 95% confidence limits: F = 6.39, t = 2.57.

effect of both Au NPs and α-MoO_3. Moreover, fine overlap between UV–vis spectra of α-MoO_3-Au and ECL emission spectra of Ru–In_2S_3 was further demonstrated the dual-quenching effect. Besides, the specific capturer H7 was applied to achieve site-oriented antibody capturing, which not only greatly improved the antibodies incubation, but also further promoted the sensitivity of the biosensor. This ECL biosensor obtained sensitive response by using PCT as a target with low detection limit of 12.49 fg/mL (S/N = 3) and wide linear range from 0.0001 to 50 ng/mL in human serum detection, indicating the established system would play a certain role and develop potential in the related further research.

Declaration of competing interest

☒ The authors declare that they have no known competing financial interests or personal relationships that could have appeared to influence the work reported in this paper.

CRediT authorship contribution statement

Jingwei Xue: Conceptualization, Data curation, Investigation, Visualization, Writing - original draft. **Lei Yang:** Formal analysis, Methodology. **Yue Jia:** Formal analysis, Methodology. **Yong Zhang:** Supervision, Writing - review & editing. **Dan Wu:** Supervision, Writing - review & editing. **Hongmin Ma:** Supervision, Writing - review & editing. **Lihua Hu:** Conceptualization, Formal analysis, Methodology. **Qin Wei:** Project administration, Resources. **Huangxian Ju:** Project administration, Resources.

ACKNOWLEDGMENTS

This study was supported by the National Key Scientific Instrument and Equipment Development Project of China (No. 21627809), National Natural Science Foundation of China (Nos. 21607055, 21575050, 21777056, 21505051), Jinan Scientific Research Leader Workshop Project (2018GXRC024).

Appendix A. Supplementary data

Supplementary data to this article can be found online at https://doi.org/10.1016/j.bios.2019.111524.

References

Bruce, D., Richter, M.M., 2002. Anal. Chem. 74 (6), 1340–1342.
Chen, M.M., Wang, Y., Cheng, S.B., Wen, W., Zhang, X., Wang, S., Huang, W.H., 2018a. Anal. Chem. 90 (8), 5075–5081.
Chen, S., Wu, N., Ma, L., Lin, S., Yuan, F., Xu, Z., Li, W., Wang, B., Zhou, J., 2018b. ACS Appl. Mater. Interfaces 10 (4), 3660–3667.
David, B., Richter, M.M., 2002. Anal. Chem. 74 (6), 1340–1342.
Dostalova, S., Cerna, T., Hynek, D., Koudelkova, Z., Vaculovic, T., Kopel, P., Hrabeta, J., Heger, Z., Vaculovicova, M., Eckschlager, T., Stiborova, M., Adam, V., 2016. ACS Appl. Mater. Interfaces 8 (23), 14430–14441.
Du, F.K., Zhang, H., Tan, X.C., Yan, J., Liu, M., Chen, X., Wu, Y.Y., Feng, D.F., Chen, Q.Y., Cen, J.M., 2018a. Biosens. Bioelectron. 106, 50–56.
Du, J., Wang, H., Yang, M., Zhang, F., Wu, H., Cheng, X., Yuan, S., Bing, Z., Li, K., Wang, Y., 2018b. Int. J. Hydrogen Energy 43 (19), 9307–9315.
Feng, Q.M., Shen, Y.Z., Li, M.X., Zhang, Z.L., Zhao, W., Xu, J.J., Chen, H.Y., 2016. Anal. Chem. 88 (1), 937–944.
Hao, Y., Jin, Z., Liu, D., Kai, F., Wang, G., 2018. J. Phys. Chem. C. Nano. Inter. 122 (19), 10430–10441.
Huang, Y., Long, X., Shen, D., Zou, G., Zhang, B., Wang, H., 2017. Inorg. Chem. 56 (17), 10135–10138.
Jia, Y., Yang, L., Feng, R., Ma, H., Fan, D., Yan, T., Feng, R., Du, B., Wei, Q., 2019. ACS Appl. Mater. Interfaces 11 (7), 7157–7163.
Jin, H., Huynh, T.P., Haick, H., 2016. Nano Lett. 16 (7), 4194.
Jing, Q., Feng, X., Zhao, X., Duan, Z., Pan, J., Chen, L., Liu, Y., 2018. ACS Appl. Nano. Mater. 1 (6), 2653–2661.
Li Hua, H., Xiao Li, C., Ying Ming, X., Li, S., Shu-Chang, S., Dan, Z., Run, W., 2019. J. Inorg. Mater. 34 (2), 193–200.
Liu, C.W., Wang, C., Liao, C.W., Golder, J., Tsai, M.C., Young, H.T., Chen, C.T., Wu, C., 2018a. AIP Adv. 8 (4), 5004–5006.
Liu, J.L., Tang, Z.L., Zhang, J.Q., Chai, Y.Q., Zhuo, Y., Yuan, R., 2018b. Anal. Chem. 90 (8), 5298–5305.
Luo, J.H., Cheng, D., Li, P.X., Yao, Y., Chen, S.H., Yuan, R., Xu, W.J., 2018. Chem. Commun. 54 (22), 2777–2780.
Mai, L.Q., Hu, B., Chen, W., Qi, Y.Y., Lao, C.S., Yang, R.S., Dai, Y., Wang, Z.L., 2010. Adv. Mater. 19 (21), 3712–3716.
Makaraviciute, A., Ramanaviciene, A., 2013. Biosens. Bioelectron. 50, 460–471.
Mandal, B., Aaryashree, Singh, R., Mukherjee, S., 2018. IEEE Sens. J. 18 (7), 2659–2666.
Nahar, S., Tajmir-Riahi, H.A., 1996. J. Colloid Interface Sci. 178 (2), 648–656.
Qin, W., Mao, K., Dan, W., Dai, Y., Jian, Y., Du, B., Yang, M., He, L., 2010. Sens. Actuators B Chem. 149 (1), 314–318.
Shi, C.G., Shan, X., Pan, Z.Q., Xu, J.J., Lu, C., Bao, N., Gu, H.Y., 2012. Anal. Chem. 84 (6), 3033–3038.
Taylorpiliae, R.E., Mohler, M.J., Najafi, B., Coull, B.M., 2015. Top. Stroke Rehabil. 23 (6), 393–399.
Tian, K., Li, D., Tang, T., Nie, F., Zhou, Y., Du, J., Zheng, J., 2018. Talanta 185, 446–452.
Wang, G., Wang, H., Cao, S., Xiang, W., Li, T., Yang, M., 2019. Microchim. Acta. 186 (2), 3223–3226.
Wang, H., Ma, Z., 2018. Sens. Actuators B Chem. 266, 46–51.
Wang, S., Guan, B.Y., Lu, Y., Lou, X.W.D., 2017. J. Am. Chem. Soc. 139 (48), 17305–17308.
Wu, F.F., Zhou, Y., Zhang, H., Yuan, R., Chai, Y.Q., 2018. Anal. Chem. 90 (3), 2263–2270.
Xiao, P., Jiang, D., Ju, L., Jing, J., Chen, M., 2018. Appl. Surf. Sci. 433, 388–397.
Xue, J., Yang, L., Wang, H., Yan, T., Fan, D., Feng, R., Du, B., Wei, Q., Ju, H., 2019. Biosens. Bioelectron. 133, 192–198.
Yang, M., Javadi, A., Gong, S., 2011. Sens. Actuators B Chem. 155 (1), 357–360.
Yang, X., Yu, Y.Q., Peng, L.Z., Lei, Y.M., Chai, Y.Q., Yuan, R., Zhuo, Y., 2018. Anal. Chem. 90 (6), 3995–4002.
Zhao, G., Wang, Y., Li, X., Yue, Q., Dong, X., Du, B., Cao, W., Wei, Q., 2019. Anal. Chem. 91 (3), 1989–1996.
Zhou, H., Han, T., Wei, Q., Zhang, S., 2016. Anal. Chem. 88 (5), 2976–2983.